ELSEVIER

Contents lists available at ScienceDirect

Journal of Non-Crystalline Solids

journal homepage: www.elsevier.com/locate/jnoncrysol



New insights into the indentation size effect in silicate glasses

Maryam Kazembeyki^a, Mathieu Bauchy^b, Christian G. Hoover^{a,*}

- ^a School of Sustainable Engineering and the Built Environment, Arizona State University, Tempe, AZ 85287, USA
- b Physics of AmoRphous and Inorganic Solids Laboratory (PARISlab), Department of Civil and Environmental Engineering, University of California, Los Angeles, CA 90095,



Keywords: Hardness AFM Ductility Modulus Energy dissipation

ABSTRACT

When glasses resist permanent deformations, for applications such as a windshield or the cover of a touch-screen device, it is important to understand how they respond to inelastic energy dissipation processes. Many glasses exhibit the so-called Indentation Size Effect (ISE), where the indentation hardness is dependent on the maximum force exerted on the probe. In this study, we perform microindentation on silica and soda lime silicate glasses over a wide range of maximum forces and extract the Vickers hardness by the Oliver and Pharr method. The inelastic volume responsible for dissipating the inelastic energy is decomposed into densification and plastic flow, using surface topography and annealing. We show that the ISE is intimately linked to these mechanisms. Finally, we hypothesize the cause of the ISE is an increase in plasticity in a zone of material under the indenter probe experiencing reduced viscosity due to high strain rates and shear thinning.

1. Introduction

At the scale of human interaction with glasses, failure at room temperature is widely considered to be brittle [1]. However, it has been shown that on smaller scales, permanent deformation can occur in glasses by means of a sharp contact with a diamond indentation probe [2-7] and has specifically been previously shown to be present in pure glassy SiO₂ [8], soda lime silicate glass [9-11]. Of all the mechanical properties that are of interest to glasses, the material hardness plays a critical role in determining this ductility, as it is a measure of the material resistance to permanent deformation. Historically, the hardness and amount of ductility was assumed to be a material property and dependent only on the glass composition [2,12,13]. However, as mechanical investigations grew to smaller scales, it was soon found that the hardness of glass has a dependence on the maximum pressure on the indenter probe. This phenomena, commonly referred to as the Indentation Size Effect (ISE), was also discovered to occur in other materials too, such as metals and ceramics [10,14-17]. The origin of ISE has been widely discussed in different studies and has been attributed to surface energy, subsurface cracking, friction at the indenter-material interface and dislocations [17-21], although friction has since been thought to play a very limited role once the hardness has reached a constant value, independent of the applied load [22]. Since glass has an non-crystalline structure (lack of long range order) the origin of ISE was thought to be mainly compositionally dependent, specifically on the

Deformations under the indenter can be divided into two main deformation processes: reversible, and irreversible [25]. Yamane and Mackenzie took this one step further and classified deformation of glass under induced stress into three distinct processes: elastic (classified by deformation that is instantaneously recovered after removal of the load), densification (a hemispherical area where interatomic bonding distance decreases), and plastic or shear-flow (characterized by inelastic deformation where volume is conserved) [24,26,27]. Unlike densification, which has a displacement transformation origin, shear flow is due to elastic/plastic mismatch [28,29]. When under stress, densification of the atomic structure has been found to be the dominant inelastic dissipation process for glasses with low Poisson's ratio. In contrast, plastic deformations play more of a role as the structure of the glass gets denser and is more prominent in glasses with a high Poisson's ratio [2,30,31]. Since the Poisson's ratio and hardness are both dependent on the composition of the glass, we see this as an opportunity to explore the very roots of the indentation size effect. Specifically, this investigation departs from the following points of inquiry:

- What extent do inelastic deformations play a role in the Indentation size effect in glasses?
- Can classical methods used to quantify volumes of plastic deformation and densification be used for a wide range of maximum indentation loads?

E-mail address: christian.hoover@asu.edu (C.G. Hoover).

atomic packing density of the glass [23,24].

^{*} Corresponding author.

To answer these questions, we employ a combination of microindentation with a Vickers probe, stress relaxation and Atomic Force Microscopy (AFM). The surface topographies before and after indentation are then used in an analytical method proposed by Yoshida [30] to quantify inelastic deformations. In order to simplify this investigation, we focus on maximum indentation forces small enough to ensure cracking and fracture is not a dominant energy dissipation mechanism. Material, sample preparation and methods are first presented, before the possible causes of the indentation size effect are elucidated and discussed.

2. Materials and methods

2.1. Sample preparation

Two widely available commercial silicate glass samples were used in this study: soda lime silicate glass (here noted as SLS) (percent composition by weight: 73% SiO₂, 14% Na₂O, 9% CaO, 4% MgO, 0.15% Al₂O₃ 0.03% K₂O, 0.1%Fe₂O₃, 0.02% TiO₂) in the form of a typical microscope slide 75x25x1 mm manufactured by VWR Scientific Inc., and 25.4 \times 25.4 \times 6.35 mm polished glassy silica (S) plates, (weight percent composition: > 99% SiO₂) manufactured by Technical Glass Products, Inc. All sample surfaces were smooth and free of imperfections from the manufacturer. To remove any residual internal stresses created during the manufacturing process, all glass samples were annealed prior to indentation. The annealing temperature profile consisted of heating the samples at a rate of 300 K/h until a max temperature equal to 90% of their glass transition temperature ($T_{\rm g}$) in Kelvin was reached. This sample temperature was held constant for 2 h and then furnace cooled [30,32,33].

2.2. Mechanical property assessment via indentation testing

Traditionally, the Vickers Hardness (H_V) of a material was calculated by dividing the maximum force (P_{max}) on the indenter probe by the surface area of the residual footprint, typically calculated as a function of the average diagonal length of the square residual footprint [34]. In this investigation, we use the approximation that the area A is in function of the contact depth h_c so that H_V is obtained by $H_V = P_{\text{max}}/$ $A(h_c)$ [35]. In this study, all tests were performed at room temperature (~20 °C). To avoid any effects of humidity contaminating the results, as previously shown through Fourier Transformation Infrared (FTIR) experiments [8], Iso-Propyl Alcohol (IPA) was pooled on top of the sample surface to prevent possible infiltration of water. This also ensured that H_V was load-rate independent [36], which has been previously shown to exist [9]. To avoid surface misidentification due to the IPA, the detection parameters were set to a contact stiffness rigid enough to ensure the indenter probe was in contact with the glass prior to the loading protocol initiating. All data was recorded using a Micro Combi Tester (MCT3) from Anton Paar (formerly CSM, Neuchatel, Switzerland) [37]. All indents were made with a four-sided pyramid (Vickers) indenter with a known projected area shape function $(A_c = 24.5h_c^2)$ [38], where h_c is the indentation contact depth as illustrated in Fig. 1. All indents were loaded in force-control up to their limiting maximum force $P_{\rm max}$. At the peak load, the force was held constant for 10 s before the load was removed. The loading rate prescribed ensured that the maximum load was reached at approximately 15 s. This allowed the entire grid to be performed without significant evaporation of the IPA.

On each specimen, at least 15 indents were performed for each different maximum load. The raw data output was a load versus load point displacement curve at every indentation point. Fig. 1 shows a typical load vs. load point displacement curve for SL and FS where $P_{\rm max}=50~{\rm g}$ -force (grf). The general shape of all curves was judged for consistency before extracting the material properties. In all cases, all curves were consistent and lying on top of one another and used for post processing calculations. The results were also consistent for

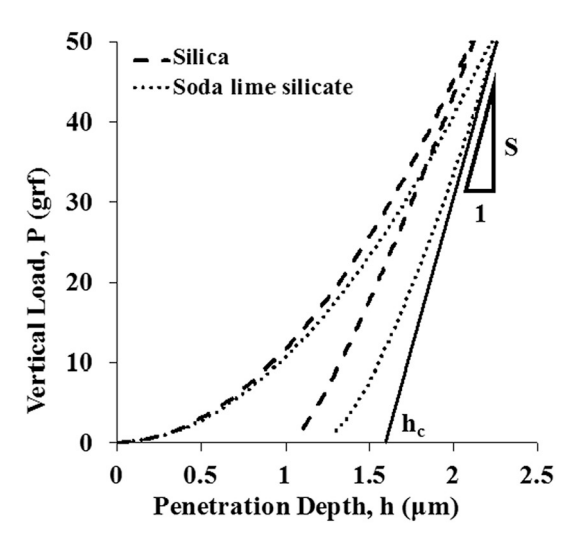


Fig. 1. Typical load vs. penetration depth (load point displacement) indentation response curve for each glass: the slope S = dP/dh and contact depth h_c is marked for soda lime silicate.

different loading/unloading times. A broad range of maximum forces were chosen to not only replicate typical load ranges in existing literature [30,36] but also to ensure that a consistent value for H_V was reached, which was only possible for higher peak forces. The range for $P_{\rm max}$ was from 12.5 grf up to 200 grf for S but only up to 100 grf for SLS. The stopping point for the force range was the limit beyond which cracking was no longer insignificant (i.e. there were discolorations in the optical images that indicated that cracking might have taken place, but the AFM images indicated that no material was "chipped" away). The indentation modulus (M) and Vickers hardness (H_V) were calculated by the software provided with the MCT3 by applying the continuum Oliver and Pharr model [35,38] using the following equations:

$$M = \frac{\sqrt{\pi}}{2} \frac{S}{\sqrt{A_{\rm c}(h_{\rm c})}} \tag{1}$$

$$H = \frac{P_{\text{max}}}{A_{\text{c}}(h_{\text{c}})} \tag{2}$$

where S = dP/dh is the measured initial slope of the unloading branch of the P-h curve, see Fig. 1; $P_{\rm max}$ is the measured maximum load at the limiting maximum penetration depth and $A_{\rm c}$ is the projected area of the indenter probe on the sample surface and is a function of the maximum contact depth, $h_{\rm c}$.

2.3. Quantifying inelastic volume deformations through AFM and annealing

The volume and topography of the residual indentation imprints were measured before and after annealing [14,30,32] by AFM. The scan was performed in contact mode at room temperature with an aluminum cantilever tip before and after the samples were annealed. Surface correction and flattening modifications included in the open source software Gwyddion were used to prepare all AFM images for analysis. Following the procedure proposed by Yoshida et al. [30], and later demonstrated for many glass compositions [11,26,39,40], the so-called volume recovery ratio ($V_{\rm R}$) and plastic shear flow deformation volume ($V_{\rm P}$) were calculated:

$$V_{\rm R} = \frac{(V_i^- - V_a^-) + (V_a^+ - V_i^+)}{V_i^-} \tag{3}$$

$$V_{\rm P} = V_i^- - ((V_i^- - V_a^-) + (V_a^+ - V_i^+))$$
(4)

where subscripts i and a indicate initial volume and volume after annealing, respectively. The superscripts – and + represent the indentation cavity volume and pile-up volume, with respect to the sample

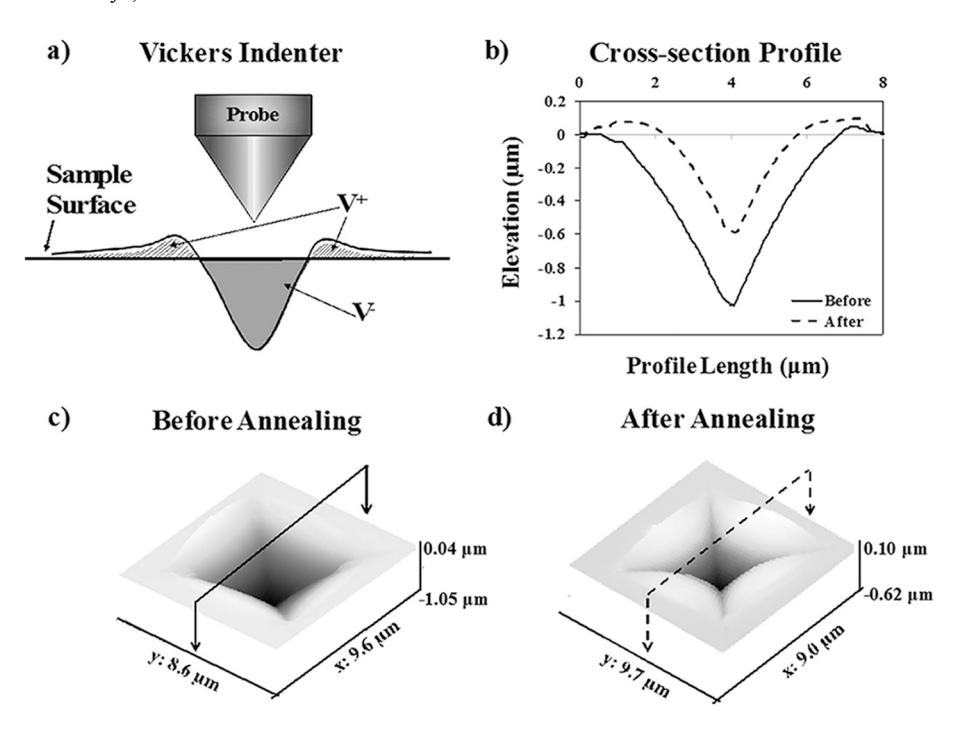


Fig. 2. (a) Schematic of a Vickers indenter and its residual impression on a sample surface. The shaded areas above and below the surface represent volumes V^+ and V^- , respectively. (b) Profiles taken along AFM images for an indent on glassy silica ($P_{max} = 50$ grf) (c) before and (d) after annealing. The profile section is shown by the solid and dashed lines in (c and d).

surface, see the cartoon in Fig. 2(a). $V_{\rm P}$ is the volume material undergoing plastic shear flow during indentation and $V_{\rm R}$ is defined as the ratio of the recovered volume during annealing with respect to the initial volume of the indentation cavity V_i^- [26,30]. In other words, the volume permanently densified ($V_{\rm d}$) during indentation can be calculated by the product of $V_{\rm R} \times V_i^-$. For better illustration of how the indent footprint changes due to the annealing process, see the before and after AFM images of the same indent on fused silica with maximum load of 50 grf in Fig. 2(c and d). Fig. 2 (b) shows an elevation view of the same cross-section that originates on opposite edges of the footprint and passes through the point of maximum penetration depth before and after annealing. The horizontal grey line in Fig. 2(b) at Elevation = 0 is the material virgin surface.

The piled-up material along the edges of the impression after the annealing process can clearly be seen. There is no considerable change in the length of the cross section diagonal dimensions after annealing, however the distance between the two opposite faces of the footprint has decreased. In addition, the deepest point in the cavity has moved closer to the elevation of the virgin surface; meaning that the densified material underneath the indenter was recovered.

3. Results

3.1. Indentation size effect on vickers hardness

The results of this investigation are summarized in Table 2, and graphically displayed in Fig. 3 through Fig. 6. The ISE on $H_{\rm V}$ for S and SLS in function of $P_{\rm max}$ in gram-force is shown in Fig. 3(a and b). The vertical lines represent the $P_{\rm max}$ where possible evidence of small closed cracks started to emerge at the corners of the indentation footprint, but there was no evidence of material being "chipped" away or lost due to a dominant fracture mechanism. The included pictures are residual footprints at various loads, showing the initial appearance of cracking at higher loads. The black circles represent the mean values from each family of tests and the error bars have length equal to twice the standard deviation of the family. The grey dashed lines are meant to just guide the eyes. It should also be noted that some of the previous studies on ISE in SLS and S have primarily been performed using probes different from a Vickers tip [8,9] and are thus not directly comparable to the results we present here.

There are two main observations considering the trends and values in Fig. 3(a and b). First, the $H_{\rm V}$ values for S are consistently larger for the same $P_{\rm max}$ when compared to SLS. This is because SLS has a larger Poisson's ratio (ν) than S (0.23 compared to 0.16) and is more compressible. This allows the indenter probe to travel deeper below the sample surface resulting in a larger contact depth ($h_{\rm c}$) and contact area ($A_{\rm c}$) and, recalling Eq. (2), a lower $H_{\rm V}$ [31,35,38]. Second, in both glasses $H_{\rm V}$ for small $P_{\rm max}$ starts off relatively large but steadily decreases and eventually becomes constant as $P_{\rm max}$ increases. The overall decrease in $H_{\rm V}$ for S is approximately 12% and for SLS is about 8%. This is consistent with what has been seen in the literature, for example in the work of Gross and Tomazawa [36]. While not a direct comparison, as their study replaced SiO₂ with equal parts CaO and Al₂O₃, they showed that any replacement of SiO₂ causes a decreased in the drop in $H_{\rm V}$ when compared to the ISE of pure SiO₂.

3.2. Evolution of V_P and V_R

Fig. 3(c and d) shows the evolution of the volume recovery ratio (V_R) and volume of plastic shear flow (V_P) . There are three main observations that concern these trends. First, the trend for V_P in both glasses follows a power law evolution in function of P_{max} . However, the quantity of V_P for S is consistently less than that of SLS by approximately a factor 3.1 for the same P_{max} ; for example, at 50 grf, V_{P} for SLS is $7.81\,\mu\text{m}^3$ and V_P for S is $2.55\,\mu\text{m}^3$. To demonstrate this, a simple power law in the form of $y = Ax^b$ was fit to the ascending trend of V_P with respect to P_{max} for both glasses, shown on a logarithmic scale graph in Fig. 4. The first two points of the S data set were excluded in order to better demonstrate that after the decrease in H_V , V_P for both glasses differ by a constant factor. The fitting was performed using the trust-region reflective algorithm [41,42] implemented in Matlab® and the optimum values for the parameters are provided in Table 1 where the uncertainty represents the 95% confidence bounds. The value of slope b for both glasses is nearly identical but the constant A for SLS is approximately 3.2 times of that for S.

The second observation is that S exhibits higher values for $V_{\rm R}$ when compared to SLS at the same $P_{\rm max}$. These observations are consistent with existing observations in literature [2,22,31,33] that describe how glasses with a higher Poisson's Ratio tends to favor plastic shear flow deformation at the expense of densification as an inelastic permanent

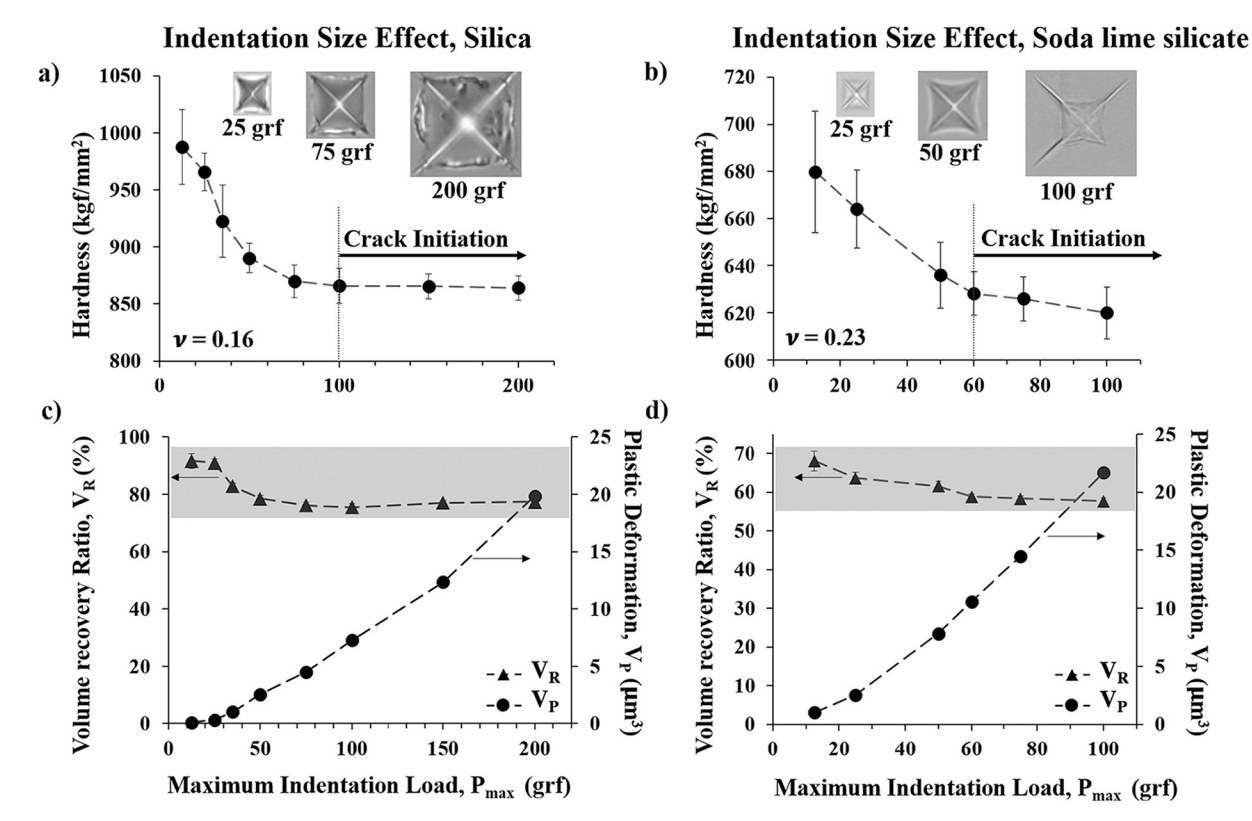


Fig. 3. Indentation size effect on Vickers hardness for (a) silica and (b) soda lime silicate glasses. (c) and (d) shows volume recovery ratio (V_R) and the volume of shear flow (V_P) for each P_{max} . The markers are means and the length of all error bars is equal to twice the standard deviation. Some error bars are hidden beneath the markers; see Table 2 for numerical values. The dashed connecting lines are only to guide the eyes and the grey boxes represent the range of V_R found in the literature. Arrows point to the y-axis for each data set.

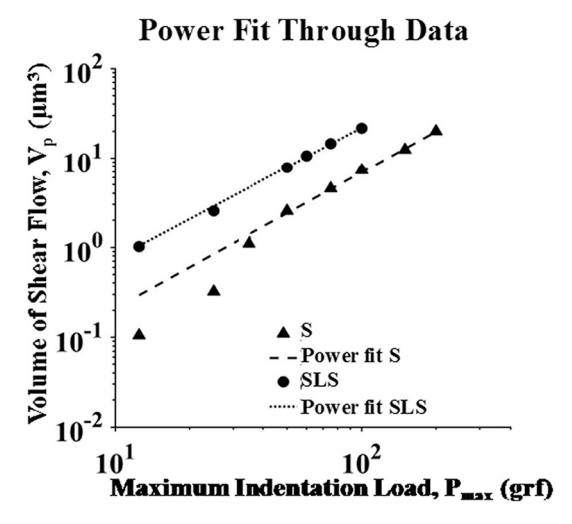


Fig. 4. Power law fitted to V_P vs. $P_{\rm max}$ curves in a logarithmic scale.

Table 1 Parameters for the fit lines ($y = Ax^b$) in Fig. 4, the uncertainty in the parameters represent the 95% confidence bounds.

	Α	b		
Silica	0.0081 ± 0.0003	1.470 ± 0.006		
Soda lime silicate	0.0258 ± 0.0094	1.464 ± 0.083		

deformation mechanism. This behavior was not unexpected and could be inferred by examining the AFM images, or cross-section profile of an indent as previously shown in [36], before annealing takes place. While not necessarily true for all materials, typically when the pile up volume is considerably small before annealing at lower loads, it is likely that densification will dominate the permanent deformation. Third, the recovered volume ratio for both glasses tends to decrease, as the indenter is pressed deeper into the material, before approaching a seemingly constant load-independent value. Though there is a wide range of values for V_R , the grey box in each graph represents the range of values for V_R as observed for SLS and S in the literature [2,30,32] and all values calculated in this study are within the range observed in previous studies. All measured and calculated values (H_V , V_P , V_R and V_d) for both glasses at each maximum force are summarized in Table 2. With these observations in mind, we seek to answer the questions posed in the beginning of this investigation.

4. Discussion

4.1. To what extent do inelastic deformations play a role in the indentation size effect in glasses?

Recalling that $V_{\rm d}$ is the product of $V_{\rm R} \times V_i^-$ and the only primary inelastic dissipation mechanisms happening at these lower loads are densification and plastic shear flow, we define the total inelastic volume under deformation as $V_{\rm in} = V_{\rm d} + V_{\rm P}$. To begin our investigation, we plot $V_{\rm in}$, $V_{\rm d}$ and $V_{\rm P}$ in function of $P_{\rm max}$, see.

Fig. 5(a and b). Following the trend for $V_{\rm P}$, both $V_{\rm in}$ and $V_{\rm d}$ also show a load dependency and follow a power law evolution in function of $P_{\rm max}$. While the trend is not so surprising, what is illuminating is the relative proportion of $V_{\rm P}$ - and $V_{\rm d}$ -to- $V_{\rm in}$. Focusing our attention to S, for $P_{\rm max} \geq 100$ grf, these relative proportions seem to be constant but this trend diverges for $P_{\rm max}$ lower than 100 grf where the largest drop in $H_{\rm V}$ is see on the ISE curve. The same trend is seen for SLS, except with the transition happening at $P_{\rm max} \geq 60$ grf. To help see this clearer, we

Table 2 Mean and standard deviation for H_V , V_P , V_R and V_d for each max indentation load P_{max} . M for silica (S) was 72.2 \pm 2.9 GPa and 74.3 \pm 4.5 GPa for soda lime silicate (SLS).

$P_{\rm max}$ (grf)	$H_V \pm \text{Std. (kgf/mm}^2)$		$V_{\rm P}~\pm~{ m Std.}~(\mu{ m m}^3)$		$V_{\rm d} \pm {\rm Std.} (\mu {\rm m}^3)$		$V_{\rm R}~\pm~{ m Std.}$ (%)		$W_{\rm in} \pm {\rm Std.} ({\rm nJ})$	
	S	SLS	S	SLS	S	SLS	S	SLS	S	SLS
12.5	987.44 ± 32	679.94 ± 25	0.1 ± 0.003	1.02 ± 0.04	1.15 ± 0.05	2.08 ± 0.11	91.67 ± 2.55	68.09 ± 3.49	13.67 ± 0.75	21.55 ± 0.55
25	963.74 ± 14	664.09 ± 16	0.32 ± 0.01	2.54 ± 0.06	3.26 ± 0.08	4.45 ± 0.15	91.00 ± 1.49	63.66 ± 1.48	40.30 ± 1.04	62.22 ± 1.68
35	922.61 ± 31	N.A.	1.01 ± 0.01	N.A.	4.92 ± 0.09	N.A.	82.8 ± 1.08	N.A.	71.70 ± 1.10	N.A.
50	890.32 ± 12	636.00 ± 14	2.55 ± 0.03	7.81 ± 0.15	9.10 ± 0.17	12.51 ± 0.35	78.54 ± 1.03	61.58 ± 1.20	117.49 ± 1.60	177.78 ± 3.26
60	N.A.	628.08 ± 90	N.A.	10.57 ± 0.14	N.A.	15.09 ± 0.27	N.A.	58.80 ± 0.76	N.A.	237.18 ± 2.75
75	870.00 ± 14	625.84 ± 90	4.52 ± 0.07	14.48 ± 0.19	14.79 ± 0.31	20.25 ± 0.37	76.10 ± 1.13	58.30 ± 0.75	217.92 ± 3.86	327.97 ± 4.32
100	865.50 ± 15	619.88 ± 11	7.25 ± 0.12	21.69 ± 0.34	22.28 ± 0.51	29.52 ± 0.66	75.44 ± 1.22	57.65 ± 0.92	336.17 ± 3.81	506.60 ± 3.21
150	865.90 ± 11	N.A.	12.35 ± 0.14	N.A.	41.56 ± 0.65	N.A.	77.10 ± 0.85	N.A.	625.67 ± 6.17	N.A.
200	864.24 ± 10	N.A.	19.84 ± 0.22	N.A.	67.68 ± 1.05	N.A.	77.33 ± 0.85	N.A.	957.70 ± 15.21	N.A.

normalize V_P and V_d by $V_{\rm in}$ and plot the inelastic volume fractions $V_P/V_{\rm in}$ and $V_d/V_{\rm in}$ vs. $P_{\rm max}$ in Fig. 5(c and d), which allows the story to begin emerging.

There are three key observations that can be discerned from these plots. First, focusing our attention again on S, it can be seen that the V_P / $V_{\rm in}$ and $V_{\rm d}/V_{\rm in}$ curves are essentially mirror reflections of each other about a horizontal line at y = 0.5, which is reassuring since their values must sum to 1 at each $P_{\rm max}$. This offers some explanation as to the wide range of V_R values abundant in the literature, bounded by the grey area in Fig. 3(c and d), as V_d is dependent on P_{max} and V_R is a function of V_d . Second, both curves appear to approach a constant value at $P_{\text{max}} \ge 100$ grf, which is exactly the same location where the ISE curve in Fig. 3(a) reaches a constant value for H_V . The third and perhaps most striking observation is that the overall shape of the $V_{\rm d}/V_{\rm in}$ curve carries a similar trend to that of the ISE curve. In fact, the location of load independency for both curves is reached at $P_{\text{max}} = 100$ grf. Additionally, the significant drop in ordinate also occurs between 25 grf and 50 grf for both curves. Similar features were also noticed in the ISE and V_d/V_{in} curves for SLS.

This prompted us to overlay the ISE curves with the V_d/V_{in} curves, which can be seen in Fig. 6(a and b). Clearly, the V_d/V_{in} curves for both glasses replicate the ISE trend quite well, within experimental scatter. This motivated us to eliminate the P_{max} axis from Fig. 6(a and b) and plot the functional relation between $H_{\rm V}$ and $V_{\rm P}/V_{\rm in}$ in Fig. 7(a and b). The results are encouraging as we find H_V decreases linearly with an increase in V_P/V_{in} . The solid black lines represent linear regression fits of the data with R² values of 0.97 and 0.95 for the S and SLS respectfully. This strongly suggests that these inelastic deformation processes play a key role in the ISE. Seeing a linear dependence of M/H on energy dissipation mechanisms is not surprising. A similar analysis was performed in [43], which showed the energy dissipation mechanisms in cement were directly linked to the densification of the cement microstructure. In fact, a similar result has been seen in white cement paste in the following reference. Specifically, the inelastic volume fractions display pressure dependence such that as P_{max} increases, the material deformation mechanism transitions away from a densification dominant mechanism and more towards a plastic shear flow mechanism for high loads. The ISE disappears once the inelastic volume fractions again

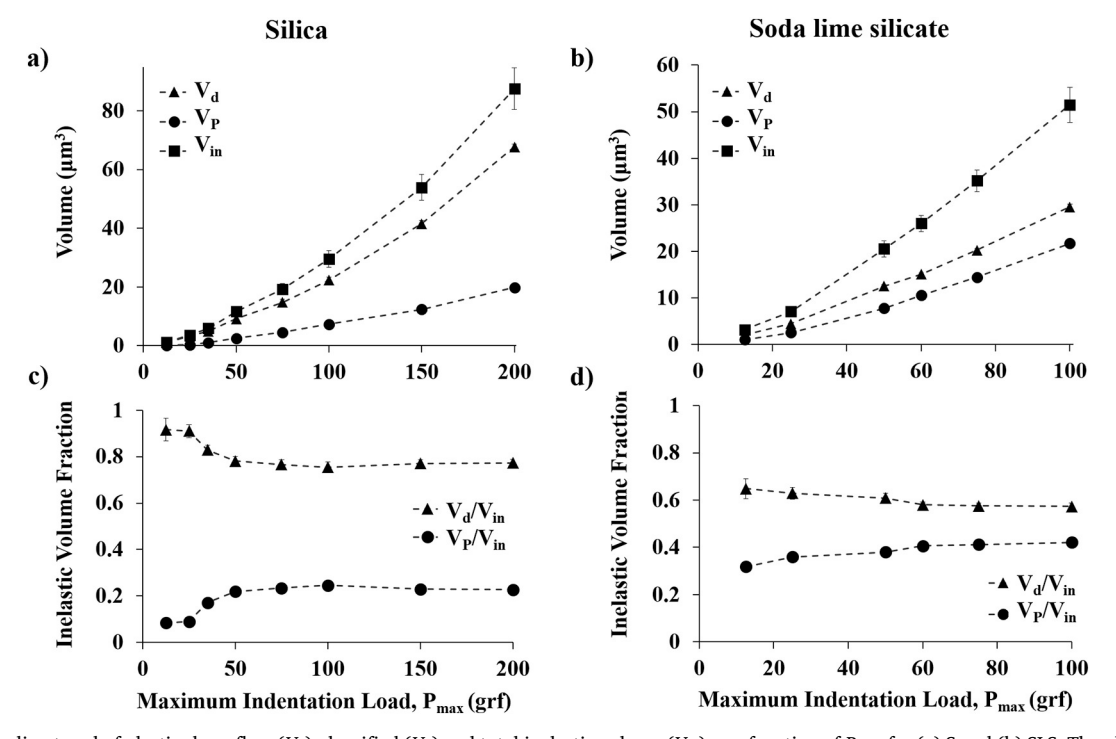


Fig. 5. The accending trend of plastic shear flow (V_p) , densified (V_d) and total inelastic volume (V_{in}) as a function of P_{max} for (a) S and (b) SLS. The plastic shear flow and densified volume normalized by the total inelastic volume with respect to P_{max} for (c) S and (d) SLS. The markers are means and the length of all error bars is equal to twice the standard deviation, which was calculated by using the first order reliability method for propagation of errors [52]. Some error bars are hidden beneath the markers.

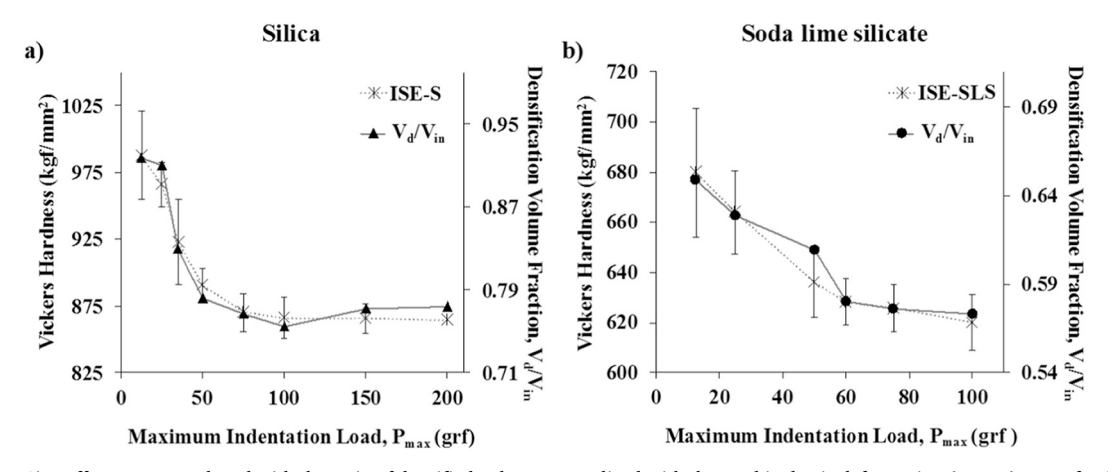


Fig. 6. Indentation Size Effect curve overlayed with the ratio of densified volume normalized with the total inelastic deformation ($V_{\rm d}/V_{\rm in}$) curve for (a) S and (b) SLS. For both plots, the solid line corresponds to the left y-axis, and the doted line corresponds to the right y-axis, respectively. The markers are means and the length of all error bars is equal to twice the standard deviation. Some error bars are hidden beneath the markers, see Table 2 for numerical values. The standard deviation for ($V_{\rm d}/V_{\rm in}$) was calculated by using the first order reliability method for propagation of errors [52].

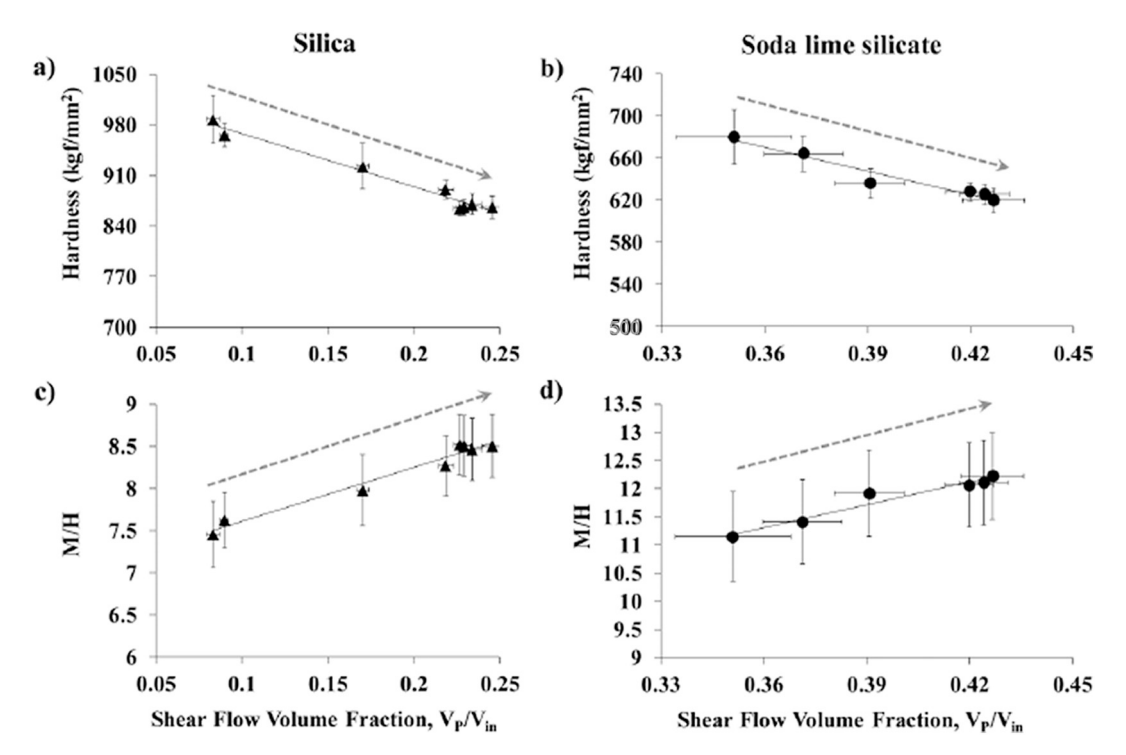


Fig. 7. a & b) Evolution of V_P/V_{in} . In function of V_P/V_{in} . c & d) Evolution of dimensionless quantities M/H in function of V_P/V_{in} . Note in (c and d), the hardness was converted from H_V to GPa. The grey arrows are to guide the eyes. The markers are means and the length of all error bars is equal to twice the standard deviation which was calculated using the first order reliability method for propagation of errors [52].

stabilize to constant values.

To further describe this relationship, one could inquire if this increase in $V_P/V_{\rm in}$ is linked to an increase in the ductility of the material. To answer this question, we turn to a measurement of ductility first considered in [44] for phase identification of heterogeneous materials, the ratio of indentation modulus over hardness (M/H) which is mechanically equivalent to the inverse of a yield strain. When a material is purely elastic, meaning no residual footprint remains after an indent is performed, M/H=2 tan(θ) = 5.59 for a Vickers probe with an equivalent half-cone angle $\theta=70.32^{\circ}$ [44]. It was later shown that greater values of M/H are indicative of an increase in plastic deformation mechanisms [43,45,46]. To apply this approach, we first convert all hardness values from Vickers to GPa. We then take the average indentation modulus M (72.2 \pm 2.9 GPa for S and 74.3 \pm 4.5 GPa for SLS) and plot M/H versus $V_P/V_{\rm in}$ in Fig. 7(c and d).

We again find that M/H scales linearly with V_P/V_{in} , which means that the ductility of each glass increases with increasing V_P/V_{in} . The solid black lines represent linear regression fits of the data with R^2 values of 0.97 and 0.95 for the S and SLS, respectively. While this link may have been intuitive, it does allow us the opportunity to define the following dimensionless relationship:

$$\frac{M}{H} = f\left(\frac{V_P}{V_{in}}\right) = m\left(\frac{V_P}{V_{in}}\right) + \gamma \tag{5}$$

Eq. (5) highlights the relationship between the ductility and the accumulation of plastic volume fraction. The apparent linear trend between these dimensionless quantities is encouraging and once this is confirmed for a larger library of glass compositions, it will be possible to define constants m and γ and relate them to other features and properties of the glass potentially allowing the ISE and $V_{\rm P}/V_{\rm in}$ to be

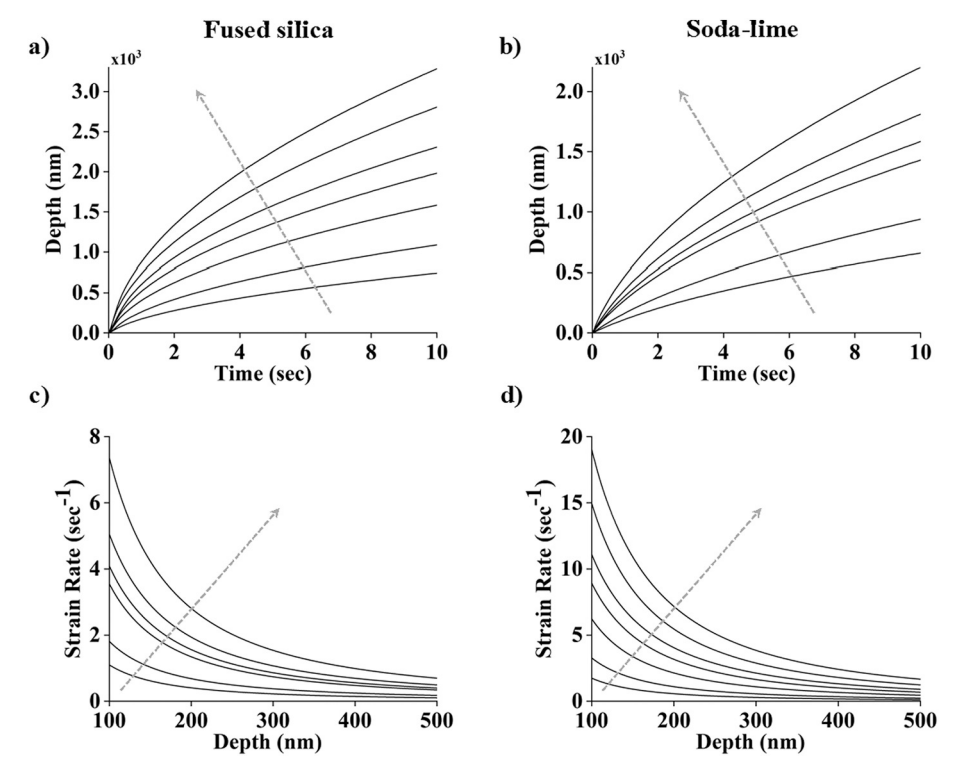


Fig. 8. Average penetration depth vs. time for entire family of a) S curves and b) SLS curves. Strain rate vs. penetration depth for entire family of a) S curves and b) SLS curves. For all figures, the dashed grey arrow is pointing in the direction of increasing P_{max} .

determined without having to perform a large battery of tests. For the SLS, m and γ are 13.4 and 6.5 respectfully. For the S, m and γ are 6.4 and 7.0 respectfully. Note that both glasses have a y-intercept > 5.59, which means that for all possible peak loads that approach $P_{\rm max}=0$, the material response will never be purely elastic and there will always be some volume of the material inelastically deforming due to plastic shear flow.

Finally, we seek to explain why the glass transitions from a densification-dominated energy dissipation mechanism under low load towards incorporating more plastic dissipation under high load. For that, we turn to Fig. 8(a and b), which show the mean penetration depth vs. time curves for each $P_{\rm max}$ during the loading phase. In these figures, it can be seen that at a given depth, the velocity (calculated as the time derivative of these curves) is increasing with increasing P_{max} . As a background, we remind ourselves of the link between stress, strain rate and viscosity. It is thus natural to hypothesize that the reason for the pressure dependence of $V_{\rm P}/V_{\rm in}$, at the expense of $V_{\rm d}/V_{\rm in}$, is caused by a change in the viscosity of the glass under the indenter probe, which is a hallmark of shear thinning [47,48]. Shear thinning is a phenomenon where at higher strain rates, the stress approaches a constant value and independent of the applied strain rate. In other words, the ratio of stress over strain rate, which is equal to the viscosity of the glass, decreases with increasing strain rates. For lower strain rates, the stress will increase proportionally with the applied strain rate, an indication of a Newtonian response. A good explanation of shear thinning can be found in [48].

We begin by first calculating the strain rates for each loading curve. Since the subsurface strain profile can be quite complex [49], we rely on the more classical definition of the average strain rate $\dot{\epsilon}$ [50]:

$$\dot{\varepsilon}(t) = \frac{d[Pd(t)]/dt}{Pd(t)} \tag{6}$$

where Pd(t) is the penetration depth at time "t". For a fixed depth, it can be seen in Fig. 8(a and b) that the velocity (slope) is higher for increasing $P_{\rm max}$, which in turn yields higher strain rates [51]. Using Eq.()

6, Fig. 8(c and d) show the strain rates as a function of penetration depth. Since Eq. (6) mathematically approaches infinity for small penetration depths, we limit our graph to penetration depths between 100 and 500 nm. We see that at any fixed depth in this range, the strain rates are increasing in function of $P_{\rm max}$. This observation leads us to the hypothesis that the viscosity of a certain zone or volume of glass under the indenter probe must decrease for increasing $P_{\rm max}$, leading to a higher accumulation of plastic shear flow volume. Based on these assumptions, this transition must occur between P_{max} of 25 and 50 grf for S and between 12.5 and 60 grf for SLS. This hypothesis is also consistent with the observation in Fig. 3(c and d) where the evolution of V_P tends to accumulate much more rapidly when H_V is decreasing.

This story suggests that the ISE arises from inelastic energy being dissipated in a greater volume fraction due to a plastic shear flow at the expense of densification. This increase in shear flow is caused by the viscosity under the indenter probe decreasing, which allows more of the glass to plastically flow. This reduction in viscosity allows the probe to travel deeper into the glass than it would have if the viscosity was to remain very high, thereby increasing the maximum depth the probe travels and decreasing $H_{\rm V}$ as it is calculated from the area of the footprint.

4.2. Applicability of Yoshida's method to determine V_P and V_R

In this study, we used the method of Yoshida to determine $V_{\rm P}$ and $V_{\rm R}$. We now seek to demonstrate that, although we had some cracking at the corners of our indents at higher loads, see Fig. 3(a and b), applying the method was still sound. First, while there was some discoloration at the corners of the indents at lower loads, there was no evidence in the AFM images that material had been "chipped away", suggesting that any cracks closed sufficiently when the Vickers probe was removed. This observation motivated us to check if energy dissipation through crack initiation and propagation was a dominant mechanism. We recall that the area under the p-h curves for each indent represents the total work done by the machine $W_{\rm T} = \int_0^{h_{\rm max}} P(s) ds$ [53].

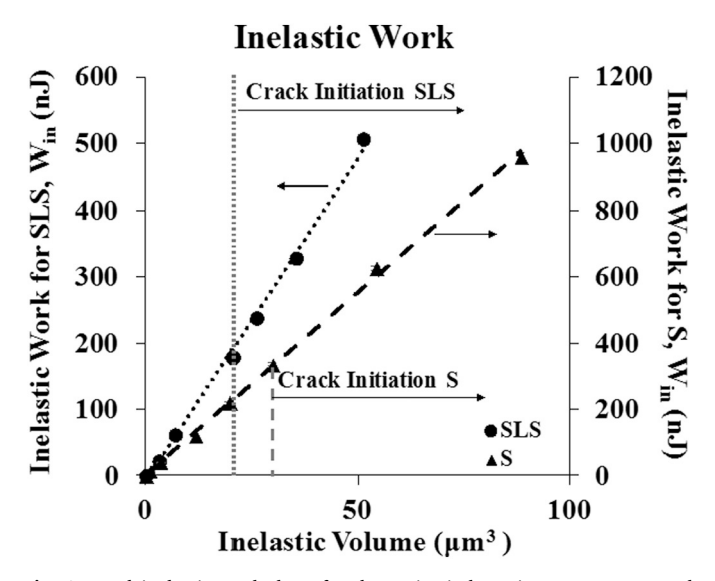


Fig. 9. Total inelastic work done for the entire indentation process vs. total inelastic volume. The arrows indicate the corresponding y-axis for each glass. The markers are means and the error bars are hidden beneath the markers; please see Table 2 for numerical values.

The elastic energy $W_{\rm E}$ is the area bounded by the unloading slope and the *x*-axis and the inelastic work $W_{\rm in}=W_{\rm T}\cdot W_{\rm E}$ [54]. These quantities were calculated by the software that came with the MCT3. The values for $W_{\rm in}$ are very consistent for each indent that the scatter bars, indicating the standard deviation for each data point, are so small and are hidden under the circles and triangles.

Fig. 9 shows the relationship between the inelastic work and inelastic volume activated for all indents performed on both glasses. The dashed lines are the linear trends through the data. If fracture was taking place, the total inelastic work would be the summation of the work done to cause $V_{\rm d}$, $V_{\rm P}$ and fracture the glass. However, this Method can only be used to determine $V_{\rm d}$ and $V_{\rm P}$ but not the volume associated with cracking. If fracture was a significant dissipation mechanism over the range of $P_{\rm max}$, the constant linear relationship between $W_{\rm in}$ and $V_{\rm in}$ would break down. Since the linear trend is uninterrupted throughout the entire dataset for both glasses, it can be assumed that, if fracture is taking place: a) the cracks must close sufficiently once the indenter probe is removed, and are thus not able to be identified by the AFM scans b) must be contributing negligibly to the total inelastic work. With this in mind, we feel that applying Yoshida's method is justified for the range of maximum loads used in this study.

5. Conclusions

The overall picture that emerges from this investigation is that the indentation size effect is intimately linked to the plastic energy dissipation mechanisms taking place during an indentation test. We demonstrated that, when indentation tests are performed on soda lime silicate and silica glasses in load control up to a maximum force, the Vickers Hardness decreases in function of increasing maximum force, which is the indentation size effect. The indents were performed with maximum loads small enough to not have fracture as a dominating energy dissipation mechanism. We also demonstrated that, through the use of Yoshida's Method, it was possible to determine the total inelastic volume used to dissipate the energy and what fraction of the inelastic volume was due to densification and plastic shear flow processes. Based on these results, we demonstrated that the ISE is intimately linked to the inelastic energy dissipation mechanisms and H_V is independent of P_{max} only when the inelastic volume fractions are also independent of P_{max} . The decrease in H_{V} is linked to the increase in ductility of the glass due to the increase in volume fraction of plastic flow. The increase in V_P

was hypothesized to be caused by a reduction in viscosity of the glass under the indenter probe due to high indentation strain rates and this was shown to be plausible as the strain rate at any depth was higher for indents with larger peak loads. The linear correlation found between M/H and $V_{\rm P}/V_{\rm in}$ is encouraging and once confirmed for a larger range of glass compositions, it could provide a valuable tool to elucidate the dependence of plastic deformation on composition. This information would provide useful input parameters for multi-scale simulations of the indentation process. Finally, we demonstrated that Yoshida's Method is applicable to use on indentation footprints when fracture is not a substantial energy dissipative mechanism, however further investigation must be performed to determine if this method is applicable when fracture is a non-negligible energy dissipative mechanism.

Declaration of Competing Interest

The authors declare that they have no known competing financial interests or personal relationships that could have appeared to influence the work reported in this paper.

Acknowledgements

This work was supported by the National Science Foundation under Grants No. 1826050, 1562066, 1762292, and 1826420.

References

- J.C. Mauro, E.D. Zanotto, Two centuries of glass research: historical trends, current status, and grand challenges for the future, Int. J. Appl. Glas. Sci. 5 (2014) 313–327, https://doi.org/10.1111/jjag.12087.
- [2] T. Rouxel, H. Ji, J.P. Guin, F. Augereau, B. Rufflé, Indentation deformation mechanism in glass: densification versus shear flow, J. Appl. Phys. 107 (2010) 094903, https://doi.org/10.1063/1.3407559.
- [3] J.T. Hagan, Shear deformation under pyramidal indentations in soda-lime glass, J. Mater. Sci. 15 (1980) 1417–1424, https://doi.org/10.1007/BF00752121.
- [4] A. Arora, D.B. Marshall, B.R. Lawn, M.V. Swain, Indentation deformation/fracture of normal and anomalous glasses, J. Non-Cryst. Solids 31 (1979) 415–428, https:// doi.org/10.1016/0022-3093(79)90154-6.
- [5] E.W. Taylor, Plastic deformation of optical glass, Nature. 163 (1949) 323, https://doi.org/10.1038/163323a0.
- [6] B. Wang, Y. Yu, M. Wang, J.C. Mauro, M. Bauchy, Nanoductility in silicate glasses is driven by topological heterogeneity, Phys. Rev. B 93 (2016) 064202, https://doi. org/10.1103/PhysRevB.93.064202.
- [7] Y.-C. Chen, Z. Lu, K. Nomura, W. Wang, R.K. Kalia, A. Nakano, P. Vashishta, Interaction of voids and nanoductility in silica glass, Phys. Rev. Lett. 99 (2007) 155506, https://doi.org/10.1103/PhysRevLett.99.155506.
- [8] K. Hirao, M. Tomozawa, Microhardness of SiO2 glass in various environments, J. Am. Ceram. Soc. 70 (1987) 497–502, https://doi.org/10.1111/j.1151-2916.1987.
- [9] A. Dey, R. Chakraborty, A.K. Mukhopadhyay, Nanoindentation of soda lime-silica glass: effect of loading rate, Int. J. Appl. Glas. Sci. 2 (2011) 144–155, https://doi. org/10.1111/j.2041-1294.2011.00046.x.
- [10] George D. Quinn, Patrice Green, Kang Xu, Cracking and the indentation size effect for knoop hardness of glasses - Quinn - 2003, J. Am. Ceram. Soc. - Wiley Online Library 86 (3) (2003) 441–448, https://doi.org/10.1111/j.1151-2916.2003. tb03319.x (accessed February 8, 2019).
- [11] P. Sellappan, T. Rouxel, F. Celarie, E. Becker, P. Houizot, R. Conradt, Composition dependence of indentation deformation and indentation cracking in glass, Acta Mater. 61 (2013) 5949–5965, https://doi.org/10.1016/j.actamat.2013.06.034.
- [12] B. Wang, Y. Yu, Y.J. Lee, M. Bauchy, Intrinsic nano-ductility of glasses: the critical role of composition, Front. Mater. 2 (2015), https://doi.org/10.3389/fmats.2015. 00011.
- [13] T. Rouxel, Elastic properties of glasses: a multiscale approach, Comptes Rendus Mécanique. 334 (2006) 743–753, https://doi.org/10.1016/j.crme.2006.08.001.
- [14] S.J. Bull, T.F. Page, E.H. Yoffe, An explanation of the indentation size effect in ceramics, Philos. Mag. Lett. 59 (1989) 281–288, https://doi.org/10.1080/ 09500838908206356.
- [15] J.B. QUINN, G.D. QUINN, Indentation brittleness of ceramics: a fresh approach, J. Mater. Sci. 32 (1997) 4331–4346, https://doi.org/10.1023/A:1018671823059.
- [16] Y.-T. Cheng, C.-M. Cheng, Scaling, dimensional analysis, and indentation measurements, Mater. Sci. Eng. R. Rep. 44 (2004) 91–149, https://doi.org/10.1016/jmser.2004.05.001.
- [17] H. Li, A. Ghosh, Y.H. Han, R.C. Bradt, The frictional component of the indentation size effect in low load microhardness testing, J. Mater. Res. 8 (1993) 1028–1032, https://doi.org/10.1557/JMR.1993.1028.
- [18] E.O. Bernhardt, On microhardness of solids at the limit of Kick's similarity law, Z Metallkd. 33 (3) (1941) 135–144.

- [19] M.V. Swain, M. Wittling, Fracture Mechanics of Ceramics, (1996), p. 355.
- [20] W.D. Nix, H. Gao, Indentation size effects in crystalline materials: a law for strain gradient plasticity, J. Mech. Phys. Solids. 46 (1998) 411–425, https://doi.org/10. 1016/S0022-5096(97)00086-0.
- [21] H. Li, R.C. Bradt, The indentation load/size effect and the measurement of the hardness of vitreous silica, J. Non-Cryst. Solids 146 (1992) 197–212, https://doi. org/10.1016/S0022-3093(05)80492-2.
- [22] T. Rouxel, Driving force for indentation cracking in glass: composition, pressure and temperature dependence, Philos. Transact. A Math. Phys. Eng. Sci. 373 (2015), https://doi.org/10.1098/rsta.2014.0140.
- [23] A.I. Priven, Methods of prediction of glass properties from chemical compositions, Glas. Glass Transit, John Wiley & Sons, Ltd, 2011, pp. 255–309, https://doi.org/ 10.1002/9783527636532.ch7.
- [24] M. Yamane, J.D. Mackenzie, Vicker's hardness of glass, J. Non-Cryst. Solids 15 (1974) 153–164, https://doi.org/10.1016/0022-3093(74)90044-1.
- [25] K. Nomura, Y.-C. Chen, R.K. Kalia, A. Nakano, P. Vashishta, Defect migration and recombination in nanoindentation of silica glass, Appl. Phys. Lett. 99 (2011) 111906, https://doi.org/10.1063/1.3637052.
- [26] J. Kjeldsen, M.M. Smedskjaer, J.C. Mauro, Y. Yue, Hardness and incipient plasticity in silicate glasses: origin of the mixed modifier effect, Appl. Phys. Lett. 104 (2014) 051913, https://doi.org/10.1063/1.4864400.
- [27] K.W. Peter, Densification and flow phenomena of glass in indentation experiments, J. Non-Cryst. Solids 5 (1970) 103–115, https://doi.org/10.1016/0022-3093(70) 90188-2
- [28] S.S. Chiang, D.B. Marshall, A.G. Evans, The response of solids to elastic/plastic indentation. I. Stresses and residual stresses, J. Appl. Phys. 53 (1982) 298–311, https://doi.org/10.1063/1.329930.
- [29] E.H. Yoffe, Elastic stress fields caused by indenting brittle materials, Philos. Mag. A. 46 (1982) 617–628, https://doi.org/10.1080/01418618208236917.
- [30] S. Yoshida, J.-C. Sanglebœuf, T. Rouxel, Quantitative evaluation of indentationinduced densification in glass, J. Mater. Res. 20 (2005) 3404–3412, https://doi. org/10.1557/imr.2005.0418.
- [31] T. Rouxel, H. Ji, T. Hammouda, A. Moréac, Poisson's ratio and the densification of glass under high pressure, Phys. Rev. Lett. 100 (2008) 225501, https://doi.org/10. 1103/PhysRevLett.100.225501.
- [32] H. Sawasato, S. Yoshida, T. Sugawara, Y. Miura, J. Matsuoka, Relaxation behaviors of Vickers indentations in soda-lime glass, J. Ceram. Soc. Jpn. 116 (2008) 864–868, https://doi.org/10.2109/jcersi2.116.864.
- [33] S. Yoshida, S. Isono, J. Matsuoka, N. Soga, Shrinkage behavior of Knoop indentations in silica and soda-lime-silica glasses, J. Am. Ceram. Soc. 84 (2001) 2141–2143, https://doi.org/10.1111/j.1151-2916.2001.tb00976.x.
- [34] A.C. Fischer-Cripps, Nanoindentation testing, in: A.C. Fischer-Cripps (Ed.), Nanoindentation, Springer New York, New York, NY, 2011, pp. 21–37, https://doi.org/10.1007/978-1-4419-9872-9
- [35] W.C. Oliver, G.M. Pharr, Measurement of hardness and elastic modulus by instrumented indentation: advances in understanding and refinements to methodology, J. Mater. Res. 19 (2004) 3–20, https://doi.org/10.1557/jmr.2004.19.1.3.
- [36] T.M. Gross, M. Tomozawa, Fictive temperature-independent density and minimum indentation size effect in calcium aluminosilicate glass, J. Appl. Phys. 104 (2008) 063529. https://doi.org/10.1063/1.2985907.
- [37] N.X. Randall, R. Christoph, S. Droz, C. Julia-Schmutz, Localised micro-hardness

- measurements with a combined scanning force microscope/nanoindentation system, Thin Solid Films 290–291 (1996) 348–354, https://doi.org/10.1016/S0040-6090(96)09184-5.
- [38] W.C. Oliver, G.M. Pharr, An improved technique for determining hardness and elastic modulus using load and displacement sensing indentation experiments, J. Mater. Res. 7 (1992) 1564–1583, https://doi.org/10.1557/JMR.1992.1564.
- [39] M. Barlet, J.-M. Delaye, T. Charpentier, M. Gennisson, D. Bonamy, T. Rouxel, C.L. Rountree, Hardness and toughness of sodium borosilicate glasses via Vickers's indentations, J. Non-Cryst. Solids 417–418 (2015) 66–79, https://doi.org/10.1016/ j.jnoncrysol.2015.02.005.
- [40] Y. Kato, H. Yamazaki, Y. Kubo, S. Yoshida, J. Matsuoka, T. Akai, Effect of B2O3 content on crack initiation under Vickers indentation test, J. Ceram. Soc. Jpn. 118 (2010) 792–798, https://doi.org/10.2109/jcersj2.118.792.
- [41] T.F. Coleman, Y. Li, An interior, trust region approach for nonlinear minimization subject to bounds, SIAM J. Optim. 6 (1996) 418–445.
- [42] T.F. Coleman, Y. Li, On the convergence of reflective Newton methods for large-scale nonlinear minimization subject to bounds, Math. Program. 67 (1994) 189-224
- [43] C.G. Hoover, F.-J. Ulm, Experimental chemo-mechanics of early-age fracture properties of cement paste, Cem. Concr. Res. 75 (2015) 42–52.
- [44] G. Constantinides, F.-J. Ulm, The nanogranular nature of C-S-H, J. Mech. Phys. Solids. 55 (2007) 64–90, https://doi.org/10.1016/j.jmps.2006.06.003.
- [45] M.J. Abdolhosseini Qomi, K.J. Krakowiak, M. Bauchy, K.L. Stewart, R. Shahsavari, D. Jagannathan, D.B. Brommer, A. Baronnet, M.J. Buehler, S. Yip, F.-J. Ulm, K.J. Van Vliet, R.J.-M. Pellenq, Combinatorial molecular optimization of cement hydrates, Nat. Commun. 5 (2014), https://doi.org/10.1038/ncomms5960.
- [46] J. Berthonneau, C.G. Hoover, O. Grauby, A. Baronnet, R.J.-M. Pellenq, F.-J. Ulm, Crystal-chemistry control of the mechanical properties of 2:1 clay minerals, Appl. Clay Sci. 143 (2017) 387–398, https://doi.org/10.1016/j.clay.2017.04.010.
- [47] D.M. Heyes, J.J. Kim, C.J. Montrose, T.A. Litovitz, Time dependent nonlinear shear stress effects in simple liquids: a molecular dynamics study, J. Chem. Phys. 73 (1980) 3987–3996, https://doi.org/10.1063/1.440624.
- [48] J.H. Simmons, What is so exciting about non-linear viscous flow in glass, molecular dynamics simulations of brittle fracture and semiconductor-glass quantum composites, J. Non-Cryst. Solids 239 (1998) 1–15, https://doi.org/10.1016/S0022-3093(98)00741-8.
- [49] M.M. Chaudhri, Subsurface strain distribution around Vickers hardness indentations in annealed polycrystalline copper, Acta Mater. 46 (1998) 3047–3056, https://doi.org/10.1016/S1359-6454(98)00010-X.
- [50] B.J. Koeppel, G. Subhash, Characteristics of residual plastic zone under static and dynamic Vickers indentations, Wear. 224 (1999) 56–67, https://doi.org/10.1016/ S0043-1648(98)00328-7.
- [51] P. Sudharshan Phani, W.C. Oliver, Ultra high strain rate nanoindentation testing, Materials. 10 (2017), https://doi.org/10.3390/ma10060663.
- [52] H.H. Ku, Notes on the use of propagation of error formulas, J. Res. Natl. Bur. Stand. Sect. C Eng. Instrum. 70C (1966) 263, https://doi.org/10.6028/jres.070C.025.
- [53] G. Constantinides, F.-J. Ulm, K. Van Vliet, On the use of nanoindentation for cementitious materials, Mater. Struct. 36 (2003) 191–196.
- [54] A.E. Giannakopoulos, S. Suresh, Determination of elastoplastic properties by instrumented sharp indentation, Scr. Mater. (1999) 1191–1198.